# Size Dependence of the Magnetic and Optical Properties of $Cd_{1-x}Mn_xS$ Nanostructures Confined in Mesoporous Silica

Felix J. Brieler,[†] Petra Grundmann,[†] Michael Fröba,*[,†] Limei Chen,[‡] Peter J. Klar,*[,‡] Wolfram Heimbrodt,[‡] Hans-Albrecht Krug von Nidda,[§] Thomas Kurz,[§] and Alois Loidl[§]

*Institute of Inorganic and Analytical Chemistry, Justus Liebig University Giessen, Heinrich-Buff-Ring 58, D-35392 Giessen, Germany, Department of Physics and Material Sciences Center, Philipps University of Marburg, Renthof 5, D-35032 Marburg, Germany, and Experimental Physics V, Electronic Correlations and Magnetism, Institute of Physics, University of Augsburg, Universitätsstrasse 2, D-86135 Augsburg, Germany*

*Received September 29, 2004. Revised Manuscript Received November 10, 2004*

Arrays of highly ordered $Cd_{1-x}Mn_xS$ nanoparticles with $x$ ranging from 0.01 to 0.2 and with lateral dimensions of 3, 6, and 9 nm were synthesized within mesoporous $SiO_2$ host structures of the MCM-41 and SBA-15 type. The hexagonal symmetry of these arrays (space group $p6m$) and the high degree of order were confirmed by X-ray diffraction and transmission electron microscope studies. Physisorption measurements show the progressive filling of the pores of the $SiO_2$ host structures, while photoluminescence excitation (PLE) and electron paramagnetic resonance (EPR) studies confirm the good crystalline quality of the incorporated $Cd_{1-x}Mn_xS$ guest species. The effects of the reduction of the lateral dimensions on the electronic properties of the diluted magnetic semiconductor were studied by PLE spectroscopy. Due to the quantum confinement of the excitons in the nanostructures an increase of the direct band gap with decreasing particle size as well as a stronger band gap bowing is observed. Analysis of the EPR line width and EPR intensity show that macroscopic magnetic properties such as the Curie−Weiss temperature are affected by the reduction of the lateral dimensions. The microscopic coupling between the Mn ions (e.g., the exchange constants $J_{nn}$ and $J_{nnn}$) is not altered to a first approximation.

## Introduction

Magnetic semiconductors are key materials for device ideas in quantum computing and spin electronics. In the early 1980s first results on doping and alloying semiconductors with magnetic ions were given.[1−4] The obtained materials, e.g., II−VI semiconductors where the cations of group II were randomly substituted by $Mn^{2+}$ ions, were called diluted magnetic semiconductors (DMS) and showed an enormous enhancement of the well-known magnetooptical effects.

The synthesis of DMS nanostructures is of great interest as semiconducting and magnetic properties are combined in one and the same nanostructure, therefore ordered arrays of nanometer-sized magnetic semiconductors are promising components for new devices in magneto- or spin electronics (e.g., magnetic hard disk media, nonvolatile computer memory chips).[5] Miniaturization of these DMS compounds leads to zero-, one-, or two-dimensional nanostructures, i.e., quantum dots, quantum wires, and quantum wells. The electronic as well as the magnetic properties of such DMS nanostructures are affected by the reduced dimensionality. These modifications of the properties are not only of interest from the point of view of fundamental physics but are also important for device performance. The smallest lateral sizes achievable by techniques such as growing structures on patterned substrates[6] or post-growth patterning and etching of the epitaxial semiconductor layers[7] are much larger than 10 nm. For the miniaturization of DMS compounds below 10 nm other methods such as incorporation of DMS clusters into silicate glass[6,8] or reverse micelles[9] or self-assembling by Stranski−Krastanov growth[10] yield cluster sizes below 10 nm, but show a much smaller degree of order.

Recently we reported on the successful incorporation of DMS compounds into the well-defined pores of hexagonally ordered mesoporous silica powders[11−14] and thin films.[15]

* Authors to whom correspondence should be addressed. E-mail: michael.froeba@anorg.chemie.uni-giessen.de or klarp@mailer.uni-marburg.de.
[†] Justus Liebig University Giessen.
[‡] Philipps University Marburg.
[§] University of Augsburg.

(1) Galazka, R. R. In *Physics of Semiconductors*; Wilson, B. L., Ed.; Institute of Physics: London, 1982; p 133.
(2) Galazka, R. R. *Lect. Notes Phys.* **1982**, *152*, 294.
(3) Gaj, J. A. *J. Phys Soc. Jpn.* **1980**, *49*, 747.
(4) Furdyna, J. K. *J. Appl. Phys.* **1982**, *53*, 7637.
(5) Prinz, G. A. *Science* **1998**, *282*, 1660.
(6) Wang, Y.; Herron, N.; Möller, K.; Bein, T. *Solid State Commun.* **1991**, *77*, 33.
(7) Klar, P. J.; Wolverson, D.; Davies, J. J.; Heimbrodt, W.; Happ, M.; Henning, T. *Phys. Rev. B* **1998**, *57*, 7114.
(8) Yanata, K.; Suzuki, K.; Oka, Y. *J. Appl. Phys.* **1993**, *73*, 4595.
(9) Levy, L.; Feltin, N.; Ingert, D.; Pileni, M. P. *J. Phys. Chem. B* **1997**, *101*, 9153.
(10) Crowell, P. A.; Nikitin, V.; Gupta, J. A.; Awschalom, D. D.; Flack, F.; Samarth, N. *Physica E* **1998**, *2*, 854.
(11) Brieler, F. J.; Fröba, M.; Chen, L.; Klar, P. J.; Heimbrodt, W. *Chem. Eur. J.* **2002**, *8*, 185.
(12) Chen, L.; Klar, P. J.; Heimbrodt, W.; Brieler, F.; Fröba, M.; Krug von Nidda, H.-A.; Loidl, A. *Physica E* **2001**, *10*, 368.
(13) Chen, L.; Klar, P. J.; Heimbrodt, W.; Brieler, F.; Fröba, M.; Krug von Nidda, H.-A.; Kurz, T.; Loidl, A. *J. Appl. Phys.* **2003**, *93*, 1326.
(14) Brieler, F. J.; Grundmann, P.; Fröba, M.; Chen, L.; Klar, P. J.; Heimbrodt, W.; Krug von Nidda, H.-A.; Kurz, T.; Loidl, A. *J. Am. Chem. Soc.* **2004**, *126*, 797.
(15) Kouzema, A. V.; Fröba, M.; Chen, L.; Klar, P. J.; Heimbrodt, W. *Adv. Funct. Mater.* **2005**, in press.

10.1021/cm048287c CCC: $30.25 
Published on Web 01/20/2005

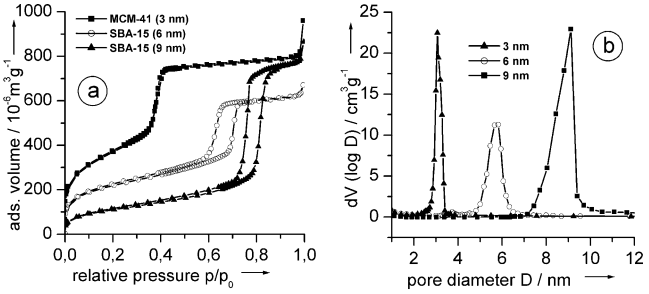


**Figure 1.** (a) $N_2$ physisorption isotherms and (b) BJH pore-size distributions (obtained from desorption branch) of the three mesoporous host structures.

Mesoporous silica materials were first introduced in 1992[16] and are well-known and studied in the field of materials science. They provide the possibility to fine-tune the pore sizes in the range of 3−50 nm[17] and can serve as a minireactor in the nanometer range for synthesizing highly ordered clusters and particles within the respective pore system in the field of host/guest chemistry. The tube-like hexagonally ordered pore systems of MCM-41 and SBA-15 enable furthermore the growing of elongated particles or even nanowires.

Here, we present the synthesis of $Cd_{1-x}Mn_xS$ with $x$ ranging from 0.01 to 0.2 inside the highly ordered pore systems of MCM-41 and SBA-15 with well-defined pore diameters of 3, 6, and 9 nm and discuss in detail the effects of size reduction on the magnetic and optical properties of the DMS guest species.

## Results and Discussion

Using powder X-ray diffraction (P-XRD), nitrogen physisorption, and transmission electron microscopy (TEM) it was possible to show that highly ordered mesoporous silicas with hexagonal symmetry of the space group *p*6*m* were synthesized.[14] Narrow pore size distributions with well-defined diameters of 3, 6, and 9 nm were obtained (see Figure 1). A high long-range order, proved by P-XRD and TEM, as well as high specific surface areas were obtained. For detailed information on synthesis procedure and characterization see refs 11−14.

**Powder X-ray Diffraction.** After the intra-pore formation of the $Cd_{1-x}Mn_xS$ guest species the mesoporous host structure was still found to be intact. In Figure 2 P-XRD patterns taken at different steps of the synthesis procedure are shown. Even after the last impregnation/conversion cycle the main peak of the silica host can still clearly be seen, whereas no reflections of the bulk sulfides are observable in the higher $2\theta$ region (not shown). This indicates a filling of the pores and a conservation of the host structure. The loss in intensity of the 100 peak of the silica host results from the increased scattering power in the pores due to the introduction of the scattering guest species. This is a well-known phenomenon in the literature.[18,19] The observed effects are the same for all incorporated samples in all three host structures.

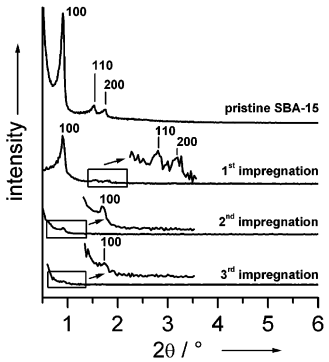


**Figure 2.** Powder X-ray diffraction patterns of pristine SBA-15 silica (6 nm pores) and a host−guest compound ($Cd_{0.95}Mn_{0.05}S$ confined in 6 nm wide pores of SBA-15 silica) after three consecutive impregnation/conversion cycles.

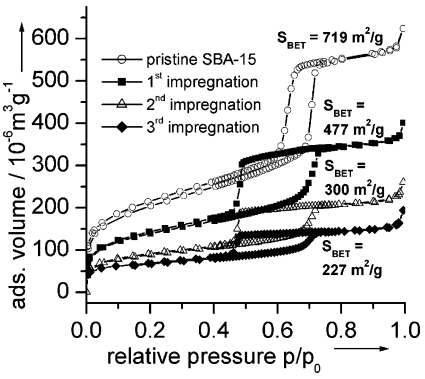


**Figure 3.** Nitrogen physisorption isotherms of pristine SBA-15 silica (6 nm pores) and of $Cd_{0.91}Mn_{0.09}S$@SBA-15 (6 nm).

**Nitrogen Physisorption.** In Figure 3 the isotherms for $Cd_{0.91}Mn_{0.09}S$@SBA-15 silica (6 nm) after the respective impregnation/conversion cycles and for the pristine SBA-15 together with the Brunauer−Emmett−Teller (BET) surface area are shown. After the intra-pore formation of the DMS compounds no change in the isotherm type (Type IV[20]) is observed, proving the conservation of the cylindrical pore system, whereas the change from H1 to H2 hysteresis indicates a partial filling of the pores. The amount of adsorbed nitrogen as well as the BET surface area are strongly reduced with increasing pore filling, i.e., number of impregnation/conversion cycles, but still mesoporosity can be found, which again proves the preservation of the mesoporous host structure and leads to the conclusion that the particles are formed inside the pores. The total pore volume calculated at $p/p_0 = 0.8$ is 0.85 cm$^3$/g for the pristine SBA-15 and 0.22 cm$^3$/g for the host/guest compound after the third impregnation/conversion cycle. This indicates a degree of filling of the pores of over 70%.

**Electron Microscopy.** Figure 4a shows exemplarily the image of a SBA-15 silica material with 6 nm wide pores. Over a wide range the high degree of order of the hexagonally arranged pores is clearly visible. In Figure 4b a

(16) Kresge, C. T.; Leonowicz, M. E.; Roth, W. J.; Vartulli, J. C.; Beck, J. S. *Nature* **1992**, *359*, 710.
(17) Zhao, D.; Feng, J.; Huo, Q.; Melosh, N.; Fredrickson, G. H.; Chmelka, B. F.; Stucky, G. D. *Science* **1998**, *279*, 548.
(18) Hammond, W.; Prouzet, E.; Mahanti, S. D.; Pinnavaia, T. J. *Microporous Mesoporous Mater.* **1999**, *27*, 19.
(19) Fröba, M.; Köhn, R.; Bouffaud, G.; Richard, O.; van Tendeloo, G. *Chem. Mater.* **1999**, *11*, 2858.
(20) Sing, K. S. W.; Everett, D. H.; Haul, R. A. W.; Moscou, L.; Pierotti, R. A.; Rouquerol, J.; Siemieniewska, T. *Pure Appl. Chem.* **1985**, *57*, 603.

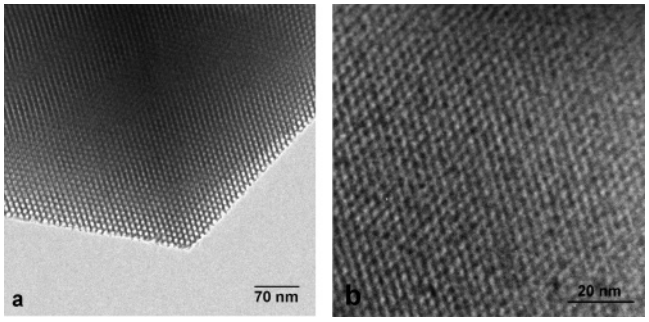


**Figure 4.** TEM images of (a) SBA-15 (6 nm pores) and (b) $Cd_{0.99}Mn_{0.01}S$@MCM-41 (3 nm pores).

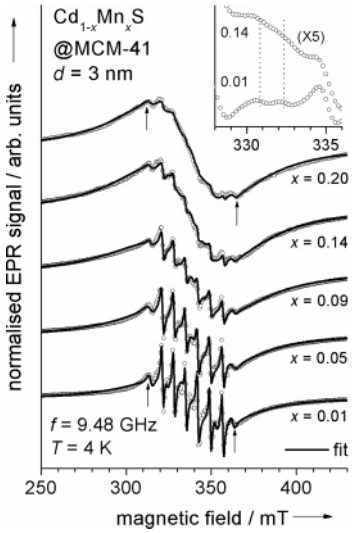


**Figure 5.** EPR spectra of 3 nm $Cd_{1-x}Mn_xS$ nanostructures within MCM-41 silica (3 nm pores) with $x = 0.01, 0.05, 0.09, 0.14, 0.2$. The fit curve consists of the field derivative of one broad Lorentz curve and two hyperfine (HF) structures. The arrows mark the wings of the second HF structure. Inset: HF transitions on an enlarged scale, dotted lines indicate the forbidden transitions.

TEM image of MCM-41 silica with incorporated $Cd_{0.99}Mn_{0.01}S$ is depicted. It can be seen that the high degree of long-range order of the pore system is preserved after incorporation of the guest material. Furthermore no particles lying on the outer surface of the silica host are present. It can be concluded that the formation of the DMS compound takes place preferentially within the pores of the respective host material. Furthermore, we pointed out elsewhere[14] that the guest species form small particles which tend to agglomerate to elongated nanoparticles inside the pore systems.

**EPR Measurements.** For all compounds EPR spectra were taken probing $Mn^{2+}$ in $Cd_{1-x}Mn_xS$. As a typical example Figure 5 shows EPR spectra of 3 nm $Cd_{1-x}Mn_xS$ samples with $x = 0.01, 0.04, 0.09, 0.14$, and 0.2, respectively. The corresponding spectra of the 6 and 9 nm nanostructures are very similar. All spectra were taken at 4 K and normalized to the same amplitude of resonance absorption. The EPR spectra are typical for exchange-coupled $Mn^{2+}$ ions in (Cd,Mn) and (Zn,Mn) chalcogenide mixed crystals.[21−23] The features in the EPR spectra can be best explained in the spectrum of the $x = 0.01$ sample. This spectrum consists of a sextet of sharp lines with a splitting of about 7 mT between neigboring lines, each line with a pair of satellites at lower magnetic field (see inset of Figure 5) on a broad background, which is well described by a Lorentzian line. The whole spectrum is centered around a $g$-factor of $g = 2.00(1)$. The sharp lines and their satellites correspond to the "allowed" ($\Delta m_S = \pm 1$, $\Delta m_I = 0$) and the "forbidden" ($\Delta m_S = \pm 1$, $\Delta m_I = \pm 1$) hyperfine transitions of the six Zeeman-splitted $m_S = -5/2, ..., +5/2$ levels of the $^6S_{5/2}$ (or $^6A_1$) ground state of the $Mn^{2+}$ 3$d$-electrons. The hyperfine structure arises from the interaction between the $S = 5/2$ spin of the unpaired 3$d$-electrons with the $I = 5/2$ spin of the $Mn^{2+}$ nucleus. The $\Delta m_S = \pm 1$ transition energies between the Zeeman levels $m_S = \pm 5/2$ and $m_S = \pm 3/2$, as well as $m_S = \pm 3/2$ and $m_S = \pm 1/2$, vary with changing crystal orientation in the range of about 2 mT with respect to the $m_S = -1/2$ to $m_S = +1/2$ transitions.[21] Therefore, the corresponding sextets of lines cannot be distinguished in the spectrum of powdered samples, but their averaging determines the width of the six resonance lines. The spectrum of $x = 0.01$ is typical for $Mn^{2+}$ ions in the tetrahedral environment of a Cd-site in a zinc blende crystal.[21,24] Thus, the crystal structure of the $Cd_{0.99}Mn_{0.01}S$ particles is zinc blende, which is often found for CdS nanoclusters containing only little manganese.[24]

With increasing $x$ the structures are smeared out due to the increasing superexchange interaction between the $Mn^{2+}$ ions.[25,26] In addition, the broad background line strongly increases and the "forbidden" hyperfine transitions become more prominent for $x \geq 0.1$. These are typical features of $Mn^{2+}$ on a Cd-site in a wurtzite crystal,[23,25] which is also tetrahedrally coordinated, but with a strong tetragonal distortion. Such a tetragonal distortion gives rise to a much stronger crystal-field splitting of the $Mn^{2+}$ ground state compared to that in a zinc blende structure. Due to the stronger crystal field the orientation-dependent EPR spectrum in wurtzite extends over a field range of about 150 mT.[21] In the powder average this yields a resonance line approximately 30 mT broad.

Besides the hyperfine structure described above, a second hyperfine structure with a larger splitting of about 9 mT can be distinguished, as indicated by the arrows in Figure 5, and gains weight with respect to the first one at higher Mn concentrations. This feature is assigned to Mn loosely aggregated at the surface of the nanostructure (it should not be confused with Mn incorporated into the crystal lattice in the vicinity of the surface). Comparing the intensity of this hyperfine structure with the total intensity allows one to estimate that in these samples the amount of Mn aggregated at the surface is less than 4% of the total Mn content in all samples. An equivalent analysis has been performed for $Zn_{1-x}Mn_xS$ nanostructures. Details can be found in ref 14.

The EPR spectrum is well fitted by the sum of the two hyperfine structures and the broad resonance line, using

(21) Schneider, J.; Sircar, S. R.; Räuber, A. *Z. Naturforsch.* **1963**, *18a*, 980.
(22) Lambe, J.; Kikuchi, C. *Phys. Rev.* **1960**, *119*, 1256.
(23) Ishikawa, Y. *J. Phys. Soc. Jpn.* **1966**, *21*, 1473.
(24) Hofmann, D. M.; Hofstaetter, A.; Leib, U.; Meyer, B. K.; Counio, C. *J. Cryst. Growth* **1998**, *184−185*, 383.
(25) Samarth, N.; Furdyna, J. K. *Phys. Rev. B* **1988**, *37*, 9227.
(26) Goede, O.; Backs, D.; Heimbrodt, W.; Kanis, M. *Phys. Status Solidi B* **1989**, *151*, 311.

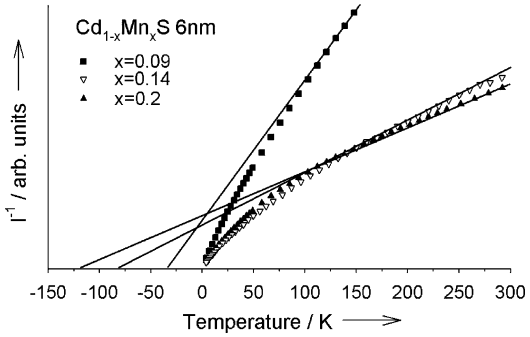


**Figure 6.** Inverse EPR intensity (corresponding to inverse susceptibility) as a function of temperature for 6 nm $Cd_{1-x}Mn_xS$ within SBA-15 silica (6 nm pores) with $x = 0.09$, 0.14, and 0.2. The negative temperature range is set for clarity. See text for explanations for $T > 100$ K.

Lorentzian line shapes. The overall intensity $I$ as well as the line width $\Delta B$ of the broad main resonance line are very sensitive to the spin−spin correlations between the $Mn^{2+}$ ions. The Curie−Weiss parameter $\Theta$ of the paramagnetic phase is a measure for the type and strength of the interaction between the Mn ions. In the mean field approximation, $\Theta$ of a $II_{1-x}Mn_xVI$ DMS can be written as[27]

$$\Theta(x) = -\frac{2}{3k_B}S(S+1)x\sum_p J_p z_p \qquad (1)$$

where $J_p$ is the exchange constant between a Mn ion and its $p$th nearest Mn neighbors and $z_p$ is the number of cations in the $p$th coordination sphere. The Curie−Weiss parameter was obtained experimentally from plots of the inverse total EPR intensity $I^{-1}$ versus temperature $T$ (the total EPR intensity is a measure of the susceptibility). At high temperatures $I^{-1}$ closely follows a Curie−Weiss dependence

$$I^{-1} \propto \chi^{-1} \propto (T + \Theta) \qquad (2)$$

At low temperatures, typically below 200 K, deviations from the Curie−Weiss behavior occur, when antiferromagnetic clustering between Mn ions starts to play a role.[28,29] This is expected as the nearest-neighbor coupling $J_1/k_B = J_{nn}/k_B$ is of the order of −10 K. It is found in the case of bulk (II,Mn)VI that the experimentally determined Curie−Weiss parameter $\Theta$ is usually well described, if the first (*nn*) and the second (*nnn*) shell of the Mn-ions are taken into account in eq 1 and higher shells are neglected,[30,31] i.e.

$$\Theta(x) = -\frac{2}{3k_B}S(S+1)x[J_{nn}z^b_{nn} + J_{nnn}z^b_{nnn}] \qquad (3)$$

For both wurtzite and zinc blende crystals, $z^b_{nn}$ and $z^b_{nnn}$ are 12 and 6, respectively, in the bulk indicated by the index $b$.

Figure 6 shows plots of the inverse EPR intensity $I^{-1}$ of 6 nm $Cd_{1-x}Mn_xS$ samples with $x$ ranging from 0.09 to 0.2 as a function of temperature. As in the case of bulk (II,Mn)VI, the slope of the $I^{-1}(T)$ curve decreases with increasing Mn-content $x$ and, at low temperatures, it deviates from the Curie−Weiss behavior giving the curves a somewhat negative curvature. Fitting the $I^{-1}(T)$ plots in the temperature regime (100−300 K) using the dependence in eq 2 yields the Curie−Weiss parameter $\Theta$ as a function of $x$. The data are summarized in Figure 7 for the 3, 6, and 9 nm $Cd_{1-x}Mn_xS$ samples. As expected, $|\Theta|$ increases with increasing $x$ in the series.

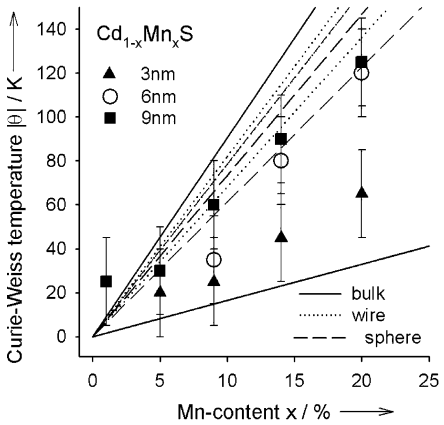


**Figure 7.** Comparison of the experimentally determined Curie−Weiss temperatures $\Theta$ of $Cd_{1-x}Mn_xS$ nanostructures confined in mesoporous silica with 3, 6, and 9 nm pores with theoretical calculations accounting for the reduction of the lateral dimensions.

The absolute $\Theta$-values obtained for the nanostructures are considerably lower than those found in corresponding bulk (II,Mn)VI samples (especially for higher $x$). The high-temperature bulk values are represented by the upper solid line in Figure 7 which is calculated using eq 3 and the exchange parameters for (Cd,Mn)S taken from the literature: $J_{nn}/k_B = -10.6$ K and $J_{nnn}/k_B = -4.7$ K.[31] The deviation of the experimental data from the bulk curve is partly due to different temperature ranges used for extracting $\Theta$, i.e., for the bulk measurements only the temperature range above 200 K was used in the literature. We used the range between 100 and 300 K to obtain comparable results for the nanostructures of different diameters and Mn concentrations. In this regime the inverse susceptibility allowed for a reasonable linear fit in all samples under investigation. As pointed out above, the absolute value of the Curie−Weiss temperature $\Theta$ decreases with decreasing temperature because the nearest neighbor Mn ions form antiferromagnetically coupled pairs, i.e., do not contribute to the magnetic properties any more. Therefore eq 3 gives an estimate of $\Theta$ at low temperatures when $J_{nn}$ is set to zero. The corresponding low-temperature bulk $\Theta$ curve is the lower solid line in Figure 7. It provides a lower boundary for the Curie−Weiss temperatures obtained in the intermediate temperature regime of the susceptibility.

Moreover, the value for $\Theta$ decreases with decreasing diameter $d$ of the nanostructures for a constant $x$. This reduction of $\Theta$ with decreasing diameter in the nanostructures occurs because Mn ions, which are situated on crystal sites in the outer layers of the (II,Mn)VI nanostructures incorporated inside the mesoporous $SiO_2$ matrixes, exhibit reduced

(27) Spalek, J.; Lewicki, A.; Tarnawski, Z.; Furdyna, J. K.; Galazka, R. R.; Obuszko, Z. *Phys. Rev. B* **1986**, *33*, 3407.
(28) Brumage, W. H.; Yarger, C. R.; Lin, C. C. *Phys. Rev.* **1964**, *133*, A765.
(29) Kreitman, M. M.; Milford, F. J.; Kenan, R. P.; Daunt, J. G. *Phys. Rev.* **1966**, *144*, 367.
(30) Furdyna, J. K.; Samarth, N.; Frankel, R. B.; Spalek, J. *Phys. Rev. B* **1988**, *37*, 3707.
(31) Chen, C.; Qu, M.; Hu, W.; Zhang, X.; Lin, F.; Hu, H.; Ma, K.; Giriat, W. *J. Appl. Phys.* **1991**, *69*, 6114.

numbers of nearest neighbors $z^s_{nn} \approx z^b_{nn}/2$ and next-nearest neighbors $z^s_{nnn} \approx z^b_{nnn}/2$ compared to the bulk of the material. This becomes significant as the surface-to-volume ratio strongly increases with decreasing $d$ in the nanostructures. The effect can be estimated by dividing the volume $V$ of the nanostructure into a volume $V^s$ close to the surface (where the exchange effects differ from bulk) and a remaining bulklike volume $V^b = V - V^s$. The choice of the two volumes will differ for nearest neighbors and next-nearest neighbors because the length scales involved, i.e., the nearest-neighbor distance $d_{nn}$ and the next-nearest neighbor distance $d_{nnn}$, are different. In the following the wurtzite structure is approximated by a zinc blende structure for simplicity. This is a good approximation as only nearest and next-nearest neighbors are considered. It holds $d_{nn} = (1/2)^{0.5}a$ and $d_{nnn} = a$ where $a$ is the lattice constant of the zinc blende lattice. It is $a \approx 0.58$ nm for zinc blende CdS.[32] We use this value of the lattice constant for $Cd_{1-x}Mn_xS$ independent of $x$ in the following because its dependence on $x$ is not known for the zinc blende modification. Two limiting cases for the shape of the nanostructure shall be considered: (i) an ideal wire structure of infinite length and diameter $d$ and (ii) a spherical nanoparticle with diameter $d$ where $d$ is the pore diameter of the $SiO_2$ host matrix. These limits are in agreement with the observed shape of comparable $Zn_{1-x}Mn_xS$ nanostructures reported earlier.[14] One obtains the following definitions:

$$V^s_{nn} = V\left(1 - \left(\frac{d - 2d_{nn}}{d}\right)^{\delta}\right) \quad V^s_{nnn} = V\left(1 - \left(\frac{d - 2d_{nnn}}{d}\right)^{\delta}\right) \quad (4)$$

where $\delta = 2$ for infinite wires and $\delta = 3$ for spheres. In both cases it holds that $V^b_{nn} = V - V^s_{nn}$ and $V^b_{nnn} = V - V^s_{nnn}$. Rewriting eq 3 including surface effects yields:

$$\Theta(x,d) = -\frac{2S(S+1)x}{3Vk_B}[J_{nn}(V^b_{nn}\, z^b_{nn} + V^s_{nn}\, z^s_{nn}) + J_{nnn}(V^b_{nnn}\, z^b_{nnn} + V^s_{nnn}\, z^s_{nnn})] \quad (5)$$

Here, it is assumed that the exchange parameters are the same in both volumes, $V^s$ and $V^b$. Using eq 5 and the parameters given above, Curie−Weiss temperatures $\Theta$ have been calculated for the 3, 6, and 9 nm $Cd_{1-x}Mn_xS$ nanostructures assuming a wire-like (dotted line in Figure 7) as well as a spherical shape (dashed line in Figure 7). Comparing experimental data and the theoretical curves indicates that the latter describe the correct trends. The theoretically estimated reduction of the Curie−Weiss parameter $\Theta$ due to surface effects is, as expected, larger for spherical nanoparticles compared to wire-shaped nanoparticles. The calculated variation of $|\Theta|$ with $d$ at constant $x$ agrees well with that found in the experiment, in particular if spherical particles are assumed. The calculated absolute values of $\Theta$ are larger than those found in the experiment, but this is very likely due to the temperature effects discussed above.

In paramagnetic systems such as the (II,Mn)VI semiconductors, the EPR line width behavior depends intimately on the physics of the Mn spin−spin interactions. Figure 8 depicts plots of the EPR line width $\Delta B$ versus temperature for various 6-nm $Cd_{1-x}Mn_xS$ nanoparticle samples of different $x$. The temperature trends of $\Delta B$ for these samples can be explained qualitatively in the same fashion as for bulk (II,Mn)VI. At low temperatures, when nearest-neighbor Mn-ions have dimerized to antiferromagnetic pairs, dipolar broadening dominates for the remaining unpaired Mn-spins. With increasing temperature, an exchange-narrowing effect is observed due to the nearest-neighbor exchange at temperatures when the thermal energy is sufficient to break up antiferromagnetically coupled nearest-neighbor pairs.

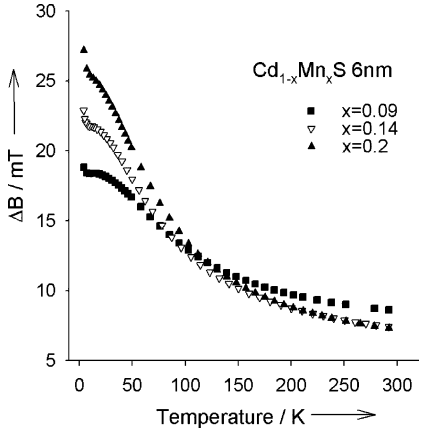


**Figure 8.** EPR line width as a function of temperature for various $Cd_{1-x}Mn_xS$ samples within SBA-15 mesoporous silica (6 nm pores).

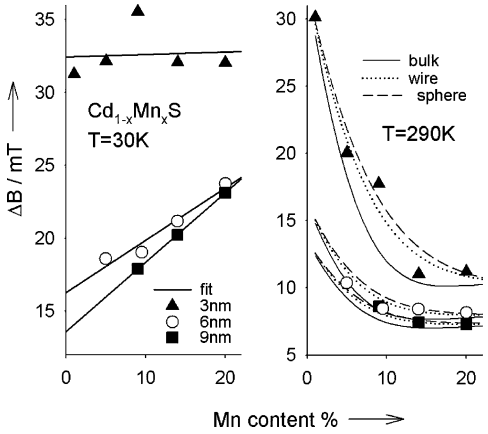


**Figure 9.** Experimentally determined EPR line width of various $Cd_{1-x}Mn_xS$ samples confined in mesoporous silica with 3 nm (▲), 6 nm (○), and 9 nm (■) pores as a function of Mn content at 30 K (left) and 290 K (right) compared with corresponding model calculations.

In the following, the concentration dependence of the line width at low temperatures ($T = 30$ K) and at high temperatures ($T = 290$ K) will be analyzed in more detail. Figure 9 shows plots of the line width at these temperatures for the 3, 6, and 9 nm $Cd_{1-x}Mn_xS$ series. It can be seen from the left graph of the figure that, at $T = 30$ K, the line width, at least for the 6 and 9 nm samples, depends almost linearly on $x$. This can be understood as follows. At these temperatures the broadening is determined by a dipolar contribution in addition to an almost constant contribution $B_{HF}$ accounting for hyperfine and crystal field effects. Exchange narrowing effects due to nearest-neighbor exchange $J_{nn}$ are negligible as basically all Mn-ions with Mn nearest neighbors have formed antiferromagnetic pairs. The line width at low temperature can be described as

(32) Landolt−Börnstein. *Numerical Data and Functional Relationships in Science and Technology*; Vol. 17b; Springer: Berlin, 1982.

$$\Delta B = B_{HF} + B_{dip} \approx B_{HF} + C_{dip}x \tag{6}$$

where $B_{dip}$ is the dipolar field at the site of a Mn-ion in mean-field approximation and $C_{dip}$ is a proportionality factor used as fitting parameter.[33] Dipolar effects seem to be smaller for the 3-nm nanostructures. Moreover, an additional constant broadening effect, the origin of which is unclear at present, occurs in these very small nanostructures. Nevertheless, the fits in the left graph of Figure 9 show that the low-temperature approximation in eq 6 well describes the observed line width behavior for the three series of samples.

The high-temperature behavior can be explained semi-quantitatively by considering the effect of the nearest-neighbor interaction $J_{nn}$, which determines the line width behavior at temperatures where the Mn nearest-neighbor pairs are broken up. For this purpose, the Mn-ions in the nanostructure can be divided into two classes: (i) isolated Mn-ions without Mn nearest neighbors (subscript *is*), and (ii) Mn-ions with one or more nearest neighbors (subscript *nn*). Furthermore, as in the case of the discussion of the Curie−Weiss parameter $\Theta$, the volume of the nanostructure will be divided into a volume close to the surface $V^s_{nn}$ and a bulklike volume $V^b_{nn}$ (see eq 4) and the discussion will again be based on a zinc blende lattice for simplicity.

The probabilities for the occurrence of the two classes of Mn-ions as a function of $x$ at the surface and in the bulk of the nanostructure are given by

$$\begin{aligned} p^b_{is} &= (1-x)^{Z_{nn}{}^b} \qquad p^b_{nn} = 1-(1-x)^{Z_{nn}{}^b} \\ p^s_{is} &= (1-x)^{Z_{nn}{}^s} \qquad p^s_{nn} = 1-(1-x)^{Z_{nn}{}^s} \end{aligned} \tag{7}$$

where $z^b_{nn} = 12$ is the number of nearest neighbors in the bulk of a zinc blende or a wurtzite lattice and $z^s_{nn} \approx z^b_{nn}/2$.

It is assumed that, in both volumes, the line width contribution $\Delta B_{is}$ of the isolated Mn-ions is well described by fits of the low-temperature line width data according to eq 6. The line width contribution of the Mn ions with nearest neighbors is calculated in the same fashion as in ref 34 but extended to account for additional broadening effects due to anisotropic exchange. In both regions it holds

$$\Delta B_{nn} = \frac{(10/3)B^2_{dip,nn} + B^2_{HF} + (B^a_{ex,nn})^2}{B^i_{ex,nn}} \tag{8}$$

where $B_{dip,nn}$ is the mean dipolar field for a Mn-ion with at least one Mn nearest neighbor. For the bulklike volume, it is defined as

$$(B^b_{dip,nn})^2 \approx \frac{3}{4}S(S+1)\mu_0{}^2\mu_B^2 g^2\left[\frac{1}{d^6_{nn}} + x^2\left(\frac{z^b_{nn}-1}{d^6_{nn}} + \frac{z^b_{nnn}}{d^6_{nnn}} + \frac{z^b_{nnnn}}{d^6_{nnnn}}\right)\right] \tag{9}$$

where only the nearest neighbors ($z^b_{nn} = 12$, $d_{nn} = (1/2)^{0.5}a$), next-nearest neighbors ($z^b_{nnn} = 6$, $d_{nnn} = a$), and third-nearest neighbors ($z^b_{nnnn} = 24$, $d_{nnnn} = (3/2)^{0.5}a$) are taken into account. In the surface region $(B^s_{dip,nn})^2$ is obtained by replacing the bulk neighbor numbers $z^b$ of each shell by the corresponding value $z^s$ for the surface region. For simplicity, all the neighbor-numbers $z^s$ are set to half the bulk value. $B_{HF}$ is the constant value for the hyperfine and crystal-field broadening determined at low temperatures for each series, and $B^a_{ex,nn}$ and $B^i_{ex,nn}$ are the anisotropic and isotropic nearest-neighbor exchange fields. The latter is calculated according to Anderson and Weiss:[34]

$$B^i_{ex,nn} = 2.83\frac{J_{nn}}{g\mu_B}\sqrt{S(S+1)} \tag{10}$$

Using $|J_{nn}| = 10.6$ K for (Cd,Mn)S yields an isotropic nearest-neighbor exchange-field of about 6 T. The total line width as a function of $x$ and diameter $d$ is calculated according to

$$\Delta B(x,d) = V^b\sqrt{(\Delta B_{is}p^b_{is})^2 + (\Delta B^b_{nn}\,p^b_{nn})^2} + V^s\sqrt{(\Delta B_{is}p^s_{is})^2 + (\Delta B^s_{nn}\,p^s_{nn})^2} \tag{11}$$

$B^a_{nn}$ is the only free parameter in the calculation. Its value is basically determined by the line width limit at high $x$ in the right graph of Figure 9. The calculations were carried out for bulk as well as for spherical and wire-like nanostructures. A constant value for the anisotropic exchange field $B^a_{nn}$ was used throughout each series. The best agreement was obtained for $B^a_{nn} = 250$, 220, and 210 mT for the 3, 6, and 9 nm series, respectively. This suggests that the anisotropic nearest-neighbor exchange-field increases slightly with decreasing diameter of the nanostructures. The values for $B^a_{nn}$ are about 1 order of magnitude larger than the corresponding dipolar field $B^b_{dip,nn}$ for $x = 0.3$ in reasonable agreement with the theoretical findings of Larson and Ehrenreich.[35]

The theoretical curves for the three $Cd_{1-x}Mn_xS$ series are also plotted in Figure 9. It can be seen that the agreement between theory and experiment is slightly better, if a spherical shape of the magnetic nanoparticles is assumed. In particular for the 3 nm series, the line width decrease with increasing $x$ is too rapid when a bulklike situation is considered. The corresponding slope is reduced by surface effects as the probability for Mn ions with Mn nearest neighbors is much lower in the surface region $V^s_{nn}$ than in the bulklike volume $V^b_{nn}$ for $0 < x < 0.2$.

**Photoluminescence and Photoluminescence Excitation Spectroscopy.** Figure 10 depicts photoluminescence excitation (PLE) spectra of the excitonic region of $Cd_{0.99}Mn_{0.01}S$ samples in 3, 6, and 9 nm porous $SiO_2$ at $T = 10$ K. The spectra were detected on the yellow Mn-related photoluminescence (PL) shown in the inset exemplarily for the 3 nm sample. This yellow band is characteristic for a Mn-ion on a cation site of a II−VI semiconductor. It originates from the $^4T_1$ to $^6A_1$ transition within the half-filled Mn $3d^5$ shell. Due to the efficient energy transfer from the semiconductor band states into the Mn subsystem there is no direct band-gap related luminescence detectable in the PL spectra. However, the efficient energy transfer allows one to detect

(33) Van Vleck, J. H. *Phys. Rev.* **1948**, *74*, 1168.
(34) Anderson, P. W.; Weiss, P. R. *Rev. Mod. Phys.* **1953**, *25*, 269.
(35) Larson, B. E.; Ehrenreich, H. *Phys. Rev. B* **1989**, *39*, 1747.

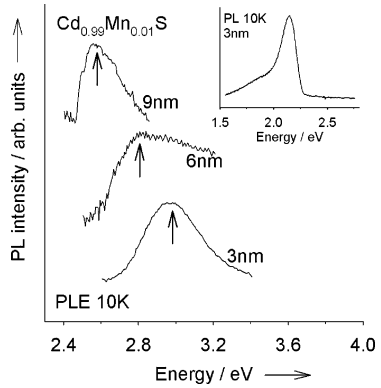


**Figure 10.** Photoluminescence excitation spectra of the excitonic region of $Cd_{0.99}Mn_{0.01}S$ samples in 3, 6, and 9 nm mesoporous $SiO_2$ detected on the yellow Mn-related luminescence (shown in the inset exemplarily for the 3 nm sample) at $T = 10$ K.

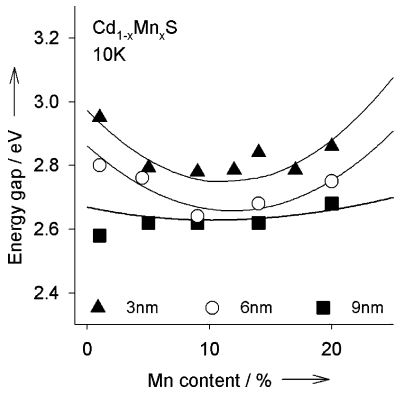


**Figure 11.** Band gap variation for $Cd_{1-x}Mn_xS$ particles confined in mesoporous silica with 3, 6, and 9 nm pores with different Mn concentrations $x$ at $T = 10$ K. The corresponding solid lines are guides to the eye.

the band gap energies of the DMS compounds in the excitation spectra. The three PLE spectra clearly indicate the increase in band gap due to quantum confinement with decreasing pore diameter.

Figure 11 summarizes the variation of the band-gap dependence on the particle size and Mn concentration $x$, extracted from the PLE spectra taken at 10 K. It can be seen clearly that confinement effects increase with decreasing particle diameter. The confinement energy is about 400 meV for the 3 nm particles. This is significantly larger than for $Zn_{1-x}Mn_xS$ nanoparticles with similar diameters, where the confinement energy was reported to be 150 meV.[14] This is due to the fact that from $Cd_{1-x}Mn_xS$ to $Zn_{1-x}Mn_xS$ the band-gap difference between the manganese doped II−VI semiconductor and $SiO_2$ as well as the exciton Bohr radius is decreasing. The energies of the band-to-band transition of the 9 nm particles are close to (or within the experimental error equal to) the corresponding bulk values, i.e., confinement effects are very small.

An interesting result is that the nanostructured systems exhibit a larger bowing of the band gap depending on the Mn-concentration than the corresponding bulk samples. The band gaps for the 6 and 9 nm $Cd_{0.99}Mn_{0.01}S$ nanostructures are not considered in this context as these samples have a zinc blende structure and not a wurtzite structure and the band gap of zinc blende CdS is known to be several tens of meV lower than that of wurtzite CdS. The band-gap dependences on Mn-content agree with the results reported for (Cd,Mn)S quantum dots by Levy et al.,[9] who also showed that the exchange interaction-induced band-gap bowing becomes stronger with decreasing diameter for (Cd,Mn)S quantum dots. Such a bowing is known for various bulk wide-gap (II,Mn)VI.[36−39] Bylsma et al. derived the following expression for the band gap as a function of temperature $T$ and Mn-concentration $x$ in DMS:[40]

$$E_g(x,T) = E_0 + \Delta E x - \frac{AT^2}{T+B} - C\chi T \qquad (12)$$

where the first three terms represent the commonly used description of the energy gap of a semiconductor alloy comprising a linear shift in composition and a Varshni-like temperature dependence. The last term is specific to DMS and causes the bowing. It describes a contribution due to the magnetic susceptibility $\chi$ of the Mn ions. Both the coupling constant $C$ and magnetic susceptibility $\chi$ may be affected by the reduction of the lateral dimensions. The coupling constant $C$ is given by

$$C \propto 3m_c\alpha^2 + \left(m_{hh} + \frac{2}{3}m_{lh}\right)\beta^2 \qquad (13)$$

where $m_c$, $m_{hh}$, and $m_{lh}$ are the conduction-band and valence-band masses and $\alpha$ and $\beta$ are the $s-d$ and $p-d$ coupling parameters. As $\alpha \ll \beta$ and $m_{hh}$, $m_{lh} > m_c$ in (II,Mn)VI, the magnitude of $C$ is mainly determined by $\beta$ for which Larson et al. give the following expression:[41]

$$\beta = -32\frac{V_{pd}^2}{N_0}\left[\frac{1}{E_v + U_{eff} - E_{3d}} + \frac{1}{E_v - E_{3d}}\right] \qquad (14)$$

where $V_{pd}$ and $U_{eff}$ are a hopping parameter depending on the manganese-anion distance and an electron−electron interaction parameter in the Hubbard fashion, respectively. $E_v$ and $E_{3d}$ are representative energies of the $p$-like valence-band edge states and the Mn 3$d$ related valence-band states, respectively.

It can be seen from eq 14 that $\beta$ strongly depends on the energy separation between the $p$-like and $d$-like valence-band states. Thus, a possible contribution to the enhanced band-gap bowing in the nanostructures is an increase of the $p-d$ exchange interaction caused by modified positions of the $p$- and $d$-related bands in the bandstructure of the nanostructures compared to bulk. Due to the quantum confinement, the lowest valence-band state of the $Cd_{1-x}Mn_xS$ nanostructures may shift significantly toward the Mn 3$d$ states, which are positioned about 3 eV below the valence-band edge of bulk material. This enhancement effect is similar to that in bulk $Cd_{1-x}Mn_xY$ with Y = Te, Se, S where an increased $p-d$ hybridization is observed with increasing band gap going

(36) Twardowski, A.; Swiderski, P.; von Ortenberg, M.; Pauthenet, R. *Solid State Commun.* **1984**, *50*, 509.
(37) Twardowski, A.; Dietl, T.; Demianiuk, M. *Solid State Commun.* **1983**, *48*, 845.
(38) Tsai, C. T.; Chen, S. H.; Chuu, D. S.; Chou, W. C. *Phys. Rev. B* **1996**, *33*, 8207.
(39) Ikeda, M.; Itoh, K. Sato, H. *J. Phys. Soc. Jpn.* **1968**, *25*, 455.
(40) Bylsma, R. B.; Becker, W. M.; Kossut, J.; Debska, U. *Phys. Rev. B* **1986**, *33*, 8207.
(41) Larson, B. E.; Hass, K. C.; Ehrenreich, H.; Carlson, A. E. *Phys. Rev. B* **1988**, *37*, 4137.

from Te to S.[42] Similar results were also reported for the corresponding Zn-series where the main Mn 3*d* photoemission feature was found at 3.5, 3.6, and 3.8 eV below the valence-band maximum of (Zn,Mn)Te, (Zn,Mn)Se, and (Zn,Mn)S, respectively.[43]

The susceptibility $\chi$ itself is also affected by the reduced dimensionality. In virtual crystal and mean-field approximation, the expression for $\chi$ is given by

$$\chi = x_{eff}\frac{N_A S(S+1)g^2\mu_B{}^2}{3k_B(T+\Theta(x))} \tag{15}$$

$x_{eff}$ (which is an magnetically effective Mn concentration accounting for antiferromagnetic pairing) as well as $\Theta(x)$ are modified in a nanostructure due to the increase of the surface-to-volume ratio. The number of nearest neighbors on the cation sublattice is reduced at the surface leading to an increase of the effective $x$ and a reduction of the Curie−Weiss parameter $\Theta$ in a similar fashion as shown for high temperatures. The combination of both effects results in a stronger increase of $\chi$ with $x$ in the nanostructures compared to bulk. Therefore, both the dependence of the $p-d$ exchange parameter $\beta$ and that of the susceptibility $\chi$ on reduced dimensionality are in concordance with the observed enhancement of the band-gap bowing in $Cd_{1-x}Mn_xS$ nanostructures as a function of $x$. However, it is worth mentioning that the dependence of the band gap of bulk $Zn_{1-x}Mn_xS$ and the corresponding nanostructured samples on Mn-concentration $x$ seems to be an exception from a general rule. Although bulk (Zn,Mn)Te[44,45] as well as (Zn,Mn)Se[41,46] exhibit considerable bowing effects, neither the bulk $Zn_{1-x}Mn_xS$[47] nor corresponding nanostructured samples in ref 14 exhibit significant bowing effects with increasing $x$.

## Conclusions

We have synthesized and thoroughly characterized $Cd_{1-x}Mn_xS$ nanoparticles with $x$ ranging from 0 to 0.2 incorporated inside mesoporous $SiO_2$ matrixes with pore sizes of 3, 6, and 9 nm. By careful characterization of the samples we demonstrate that under these synthesis conditions most of the Mn ions are incorporated on cation sites of the CdS lattice and that the amount of Mn aggregated at the surface of the nanostructures is negligible. This allows us to thoroughly investigate the effects of reduced dimensionality on the magnetic and electronic properties of the $Cd_{1-x}Mn_xS$ nanoparticles as a function of Mn content $x$ and characteristic diameter $d$. Both magnetic and electronic properties of the nanoparticles are modified due to the reduced lateral dimensions. We demonstrate by analysis of the EPR line width and EPR intensity that macroscopic magnetic properties such as the Curie−Weiss temperature are strongly affected by the reduction of the lateral dimensions, whereas the microscopic coupling between the Mn ions (e.g., the exchange constants $J_{nn}$ and $J_{nnn}$) is not altered to a first approximation. The macroscopic modifications arise mainly due to geometrical restrictions, i.e., the number of neighbors in the cation shells around a Mn-ion in the surface region is considerably reduced compared to that of a Mn ion in the bulk. Due to the quantum confinement of the excitons in the nanostructures an increase of the direct band gap with decreasing particle size is observed. Furthermore, the band gap bowing as a function of Mn content $x$ is enhanced with decreasing nanostructure diameter $d$. This enhanced band gap bowing can also be related to the alterations of the macroscopic magnetic properties (i.e., reduction of Curie−Weiss temperature $\theta(x)$ and increase of effective Mn-concentration $x_{eff}$) which occur due to the increase of the surface-to-volume ratio with decreasing nanostructure size.

## Analyses and Measurements

Powder X-ray diffraction (P-XRD) patterns were recorded at room temperature with a Bruker AXS D8 Advance diffractometer (Cu K$\alpha$) in $\theta/\theta$ geometry with a secondary monochromator.

Physisorption measurements were carried out using Quantachrome Autosorb 1 and Autosorb 6 instruments with nitrogen as adsorptive at 77 K. The BET surface areas were calculated from $p/p_0 = 0.03-0.3$ in the adsorption branch, and the BJH pore size distributions were calculated from the desorption branch. Before each sorption measurement the sample was outgassed at 120 °C for at least 24 h under turbomolecular pump vacuum.

For electron microscopic measurements the samples were prepared by dipping a holey copper grid into the dried and finely ground powders. The transmission electron micrographs were recorded on a Philips CM 300 UT and on a Philips CM 30 ST.

The photoluminescence-based optical measurements were carried out at 10 K with the specimen mounted in a contact-gas He-cryostat (Cryovac K 1104 C). Tuneable monochromatic excitation light with a bandwidth of 5 nm was provided either by a tungsten lamp (for PLE measurements) or by a Xenon lamp (for PL measurements) followed by a 0.32 m monochromator (ISA Triax 320). The sample luminescence was detected using a 0.5 m spectrometer (Zeiss) with a resolution better than 1 nm equipped with a GaAs photomultiplier (Hamamatsu). For the PL measurements the sample was excited with the lamp system set to 420 nm (2.95 eV). The PL signal was detected in the range from 500 to 700 nm. For the photoluminescence excitation (PLE) measurements the PL intensity was detected at 580 nm varying the wavelength of the excitation light from 270 to 560 nm.

Electron paramagnetic resonance (EPR) measurements were performed using a Bruker Elexsys 500 CW spectrometer at X-band frequencies (9.48 GHz) and magnetic fields up to 1 T at temperatures between 4 and 300 K in a continuous-flow He cryostat (Oxford Instruments). As the signal-to-noise ratio was improved by a lock-in technique with field modulation, the EPR spectra represented the field derivative of the microwave power absorbed by the sample from the transverse magnetic microwave field as a function of the external static magnetic field.

**Acknowledgment.** We thank Günter Koch (Institute of Inorganic and Analytical Chemistry, Justus Liebig University Giessen) for the transmission electron micrographs. Financial

(42) Taniguchi, M.; Fujimori, M.; Fujisawa, M.; Mori, T.; Souma, I.; Oka, Y. *Solid State Commun.* **1987**, *62*, 431.
(43) Weidemann, R.; Gumlich, H.-E.; Kupsch, M.; Middelmann, H.-U.; Becker, U. *Phys. Rev. B* **1992**, *45*, 1172.
(44) Twardowski, A.; Swiderski, P.; von Ortenberg, M.; Pauthenet, R. *Solid State Commun.* **1984**, *50*, 509.
(45) Lee, Y. R.; Ramdas, A. K.; Aggarwal, R. L. In *Proceedings of the 18th International Conference on the Physics of Semiconductors*; World Scientific: Singapore, 1986.
(46) Twardowski, A.; Dietl, T.; Demianiuk, M. *Solid State Commun.* **1983**, *48*, 845.
(47) Theis, D. *Phys. Lett. A* **1976**, *59*, 154.

support by the Deutsche Forschungsgemeinschaft (Fr 1372/4-3 and He 2298/4-3 and SFB 484, Augsburg) and the Fonds der Chemischen Industrie is gratefully acknowledged. T.K. was supported by the EU-graduate college "Electron−Electron Interactions in Solids". This work was also partially supported by the Bundesministerium für Bildung und Forschung (BMBF) under Contract 13N6917/0 (EKM) and by the Optodynamics Center of the Philipps University.

CM048287C